Modelling of delta ferrite to austenite phase transformation kinetics in martensitic steels: application to rapid cooling in additive manufacturing

Flore Villaret, Xavier Boulnat, Pascal Aubry, Julien Zollinger, Damien Fabrègue, Yann Decarlan

► To cite this version:

Flore Villaret, Xavier Boulnat, Pascal Aubry, Julien Zollinger, Damien Fabrègue, et al.. Modelling of delta ferrite to austenite phase transformation kinetics in martensitic steels: application to rapid cooling in additive manufacturing. Materialia, 2021, 18 (2021) (101157), pp.18 (2021). 10.1016/j.mtla.2021.101157 . cea-03330729

HAL Id: cea-03330729
https://cea.hal.science/cea-03330729

Submitted on 1 Sep 2021

Modelling of delta ferrite to austenite phase transformation kinetics in martensitic steels: application to rapid cooling in additive manufacturing

Flore Villaret[a,1*], Xavier Boulnat[b], Pascal Aubry[c], Julien Zollinger[d], Damien Fabrègue[b], Yann de Carlan[a]

[a] Université Paris-Saclay, CEA, Service de Recherches Métallurgiques Appliquées, F-91191, Gif-sur-Yvette, France

[b] Université de Lyon, INSA de Lyon, MATEIS CNRS UMR 5510, F-69621 Villeurbanne, France

[c] Université Paris-Saclay, CEA, Service d'Études Analytiques et de Réactivité des Surfaces (SEARS), F-91191, Gif-sur-Yvette, France

[d] Institut Jean Lamour, CNRS – Université de Lorraine, ARTEM Campus – Allée André Guinier, F-54000 Nancy, France

*corresponding author, e-mail: flore.villaret@edf.fr, phone: +33 6 24 54 78 08

---

[1] Present adress : EDF R&D, MMC C24, Les Renardières, Moret sur Loing, F-77250 France

Declaration of interest: none

ABSTRACT

In this paper, the high temperature transformation kinetics of delta ferrite to austenite (δ → γ) phase transformation is modeled by thermodynamic and diffusion calculations. It appears that, in martensitic steels, the δ → γ transformation is very fast (a few milliseconds) as soon as the first austenite nuclei appears. Classically the austenitic phase will thus systematically be observed in the material during conventional elaboration processes. However, in powder metallurgy and additive manufacturing, it is possible to obtain sufficiently high quenching rates (up to 10^6 °C/s) so that the γ phase does not have time to appear. The calculations presented here allow to rationalize the understanding of the microstructures of powders and different additive manufacturing materials. They enable to understand why ferrite or martensite is sometimes obtained in the final microstructure. From the calculations made, an original CCT (Continuous Cooling Transformations) diagram starting from the δ phase is proposed. This understanding is one more step toward the control of microstructure and properties of additively manufactured martensitic steels.

Keywords: Steel, Martensite, Phase transformation kinetics, Electron BackScatter Diffraction (EBSD), Metal Additive manufacturing

1. INTRODUCTION

High-chromium martensitic steels are widely used in energy applications, thanks to their good mechanical and corrosion properties at high temperature and their resistance to irradiation swelling [1–4]. These steels are called martensitic because of their ability to keep a martensitic microstructure under low cooling rates, which are induced in conventional manufacturing steps, such as forging. The extreme temperature gradients and the very fast cooling rates associated with additive manufacturing processes can lead to out-of equilibrium microstructures. As reported by Herzog et al. [5], many studies have been done on austenitic stainless steels such as 316L or 304L, but only few studies deal with martensitic steels, focusing on maraging and tools steels.

As a matter of fact, steels which exhibit a martensitic microstructure with the conventional elaboration processes can exhibit a ferritic or ferritic/martensitic microstructure after additive manufacturing. Such unusual microstructures were already reported in literature. For example, in precipitation hardened steels such as the 17-4PH, Sun et al. [6] noticed that changing the laser beam path length and wall thickness in Laser Beam Powder Bed Fusion (PBF-LB) allowed to switch from a ferritic to a martensitic microstructure. In the same way, Adeyemi et al. [7] observed that increasing laser power leads to more ferrite in Laser Beam Direct Energy Deposition (DED-LB). Vunnam et al. [8] has shown that, with the same PBF-LB building parameters, a small change in the powder chemical composition can also change the microstructure.

In reduced activation 9Cr steels, Liu et al. [9] and Jiang et al. [10] observed that it is possible to control the amount of ferrite by changing the scanning strategy in

PBF-LB. Zhong et al. [11] chose instead to specifically design an alloy composition for DED-LB process to obtain the martensitic microstructure. This is also possible with the good processing conditions, as demonstrated for example in DED-LB by Xia et al. [12].

Alnajjar et al. [13], as others authors, explain the formation of this microstructure by the possibility of partially or entirely "skipping" the austenitic domain due to the high cooling rate in additive manufacturing but no model could be proposed to account for the diversity of the microstructures obtained.

In this article, the growth kinetics of an austenite nucleus as a function of the cooling rate is computed by thermodynamic and diffusion calculation. This demonstrates to what extent it is possible to avoid — or not — the formation of austenite during cooling and allow to understand the microstructures in martensitic steels obtained by additive manufacturing.

A Fe-9Cr-1Mo martensitic steel is used as a demonstration alloy. In this example, the variation of the cooling rate will be obtained by comparing different sizes of powder particles and PBF-LB and DED-LB builds. Indeed, the cooling rate is one or two magnitude order higher in PBF-LB [14].

2. EXPERIMENTAL TECHNIQUES

Samples were built using a Fe-9Cr-1Mo pre-alloyed steel powder. Chemical composition and powder size distribution used in this work are given in Table 1. This powder was gas atomised, so it has spherical particles, a microstructural analysis of the powder is presented later, in 4.2. DED-LB and PBF-LB samples were built using parameters listed in Table 2.

Fe	C	Cr	Ni	Mo	Mn	Si	N	D_{10} (µm)	D_{50} (µm)	D_{90} (µm)
Bal.	0.10	9.3	0.22	1.04	0.48	0.28	0.004	10	30	65

Table 1: Main alloying elements of the Fe-9Cr-1Mo powder (wt%).

Method	DED-LB	PBF-LB
Setup	Optomec LENS 850R	Trumpf Truprint series 1000
Laser power (P) (W)	400	100
Scanning speed (v) (mm/s)	5	200
Fe-9Cr-1Mo flow rate (g/min)	2	-
Layer height (h) (µm)	200	20
Shielding/carrying gas	Argon	Argon
Spot diameter (D_{spot}) (µm)	1400	50
Surface Energy density ($P/v.D_{spot}$) (J/mm^2)	57	10
Volume energy density ($P/v.D_{spot}.h$)(J/mm^3)	285	500
Cooling speed estimated from [14] **(°C/s)**	10^4	10^6
Scanning strategy	Single tracks	Island scan + 67° rotation between each layers
Samples geometry	Walls 20x30 mm	Cube 10x10x10 mm

Table 2: Building parameters.

The microstructure was observed on a ZEISS Sigma HD Field Emission Gun Scanning Electron Microscope (FEG-SEM) with a Bruker Electron BackScatter Diffraction (EBSD) camera with a voltage of 20 kV. In PBF-LB samples, observations were conducted in the plan parallel to the Building Direction (BD). In DED-LB samples, observations were conducted in the plan parallel to the Building Direction and the Scanning Direction.

The step size used for acquisition of all EBSD maps is 0.2 µm/pixel. Inverse Pole Figures (IPF) are projected along the building direction. A threshold angle of 10° was used to define grain boundaries. EBSD Band Contrast was used to distinguish ferrite from martensite by computing the mean band contrast by grains with the method described in [8,15–17]. An adapted threshold was then used to separate ferrite grains from martensite.

3. AUSTENITE GROWTH KINETICS MODELING DURING COOLING FROM DELTA PHASE

This section proposes a scenario to explain the microstructure differences in martensitic steels, based on the example of Fe-9Cr-1Mo powders, and steels built either by DED-LB or PBF-LB. The growth kinetics of an austenite nucleus during cooling, as a function of the cooling rate is calculated using diffusion equations. Here, each transformation temperature is named as following (see also Figure 1):

- Ae_5 for the beginning of austenite formation ($\delta \rightarrow \delta + \gamma$)
- Ae_4 for the end of austenite formation ($\delta + \gamma \rightarrow \gamma$)
- Ae_3 for the beginning of α ferrite formation ($\gamma \rightarrow \alpha + \gamma$)
- Ae_1 for the end of α ferrite formation ($\alpha + \gamma \rightarrow \alpha$)

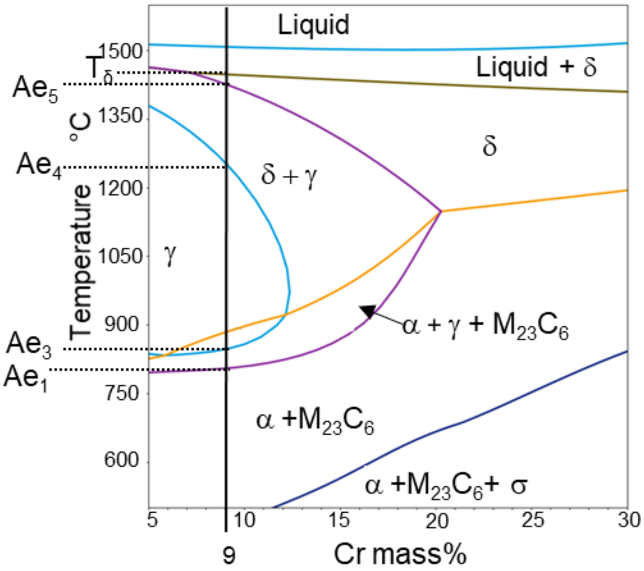

Figure 1: Pseudo-binary diagram for Fe-xCr-1Mo

Assuming that solidification takes place in the δ domain and that an austenite nucleus is instantly formed when T < Ae_5 (these assumptions will be discussed in more details later), its growth during cooling is mainly controlled by diffusion [18,19]. The idea here is to compute the size reached by an austenite grain after cooling for each process.

Since the cooling rates considered are very high, the model presented here is based on the assumption that austenite growth is controlled by the diffusion of interstitial elements such as carbon and nitrogen, while other elements do not have the time to diffuse [20]. In the case of the Fe-9Cr-1Mo steel used as an example here, the nitrogen content is very low (4 ppm of nitrogen versus 1000 ppm of carbon), so only carbon diffusion will be considered.

The growth of an austenite grain during cooling can be calculated in the δ + γ and γ domains successively.

In the δ + γ domain, the thermodynamic equilibrium of carbon distribution between the two phases must be considered. The radius $r_{\delta+\gamma}$ of a growing nucleus in this temperature range according to the cooling speed (v) can then be calculated with the following equation, adapted from [21]:

$$\boldsymbol{r_{\delta+\gamma}} = \int_{\boldsymbol{Ae_4}}^{\boldsymbol{Ae_5}} \frac{\boldsymbol{D(T).\Omega(\mathrm{T})}}{\boldsymbol{1-0.25\left(\Omega(\mathrm{T})+\sqrt{\Omega(\mathrm{T})^2+8\Omega(\mathrm{T})}\right)}}.\frac{\boldsymbol{dT}}{\boldsymbol{v}} \qquad \textbf{(1)}$$

Where $D(T)$ is the carbon diffusion coefficient in γ phase, depending on the temperature T, and Ω is the supersaturation considering local thermodynamic equilibrium defined as:

$$\boldsymbol{\Omega} = \frac{\boldsymbol{\omega_C^0 - \omega_C^{\delta/\gamma}}}{\boldsymbol{\omega_C^{\gamma/\delta} - \omega_C^{\delta/\gamma}}} \qquad \textbf{(2)}$$

Where ω_C^0 is the nominal carbon composition of the steel, $\omega_C^{\delta/\gamma}$ is the carbon concentration of δ in equilibrium with γ and $\omega_C^{\gamma/\delta}$ is carbon concentration of γ in equilibrium with δ.

These carbon equilibrium contents of the δ and γ phases in the δ + γ domain, as well as the diffusion coefficients as a function of temperature are obtained from the data tabulated in the ThermoCalc software with the TCFE5 and MOB2 thermodynamic and mobility databases.

In the γ domain, the growth of the nucleus is only controlled by atomic diffusion, the final size r_f of the new grain when Ae_3 is reached is calculated according to the cooling speed using the following equation (adapted from [19]):

$$\boldsymbol{r_f = r_{\delta+\gamma} + \int_{Ae_3}^{Ae_4} 2\left(D(T).\frac{dT}{v}\right)^{0.5}} \qquad \textbf{(3)}$$

To carry out these calculations, the Fe-9Cr-1Mo equilibrium phase diagram is used. The calculated two-phase δ + γ domain therefore extends from Ae_5 = 1420 °C to Ae_4 = 1240 °C, and the single-phase γ domain from Ae_4 = 1240 °C to Ae_3 = 850 °C (Figure 1).

With this input data and using equations (1) and (3), it is possible to plot the size of an austenite grain when it reaches Ae_3 as a function of the cooling rate (green curve in Figure 2). To test another hypothesis than a nucleus immediately formed at Ae_5, other calculations have been made assuming that the austenite grain only forms at 1200 °C (red curve on Figure 2) or 1100 °C (blue curve on Figure 2). As expected, the size of the austenite grain is then much smaller when the temperature reaches Ae_3.

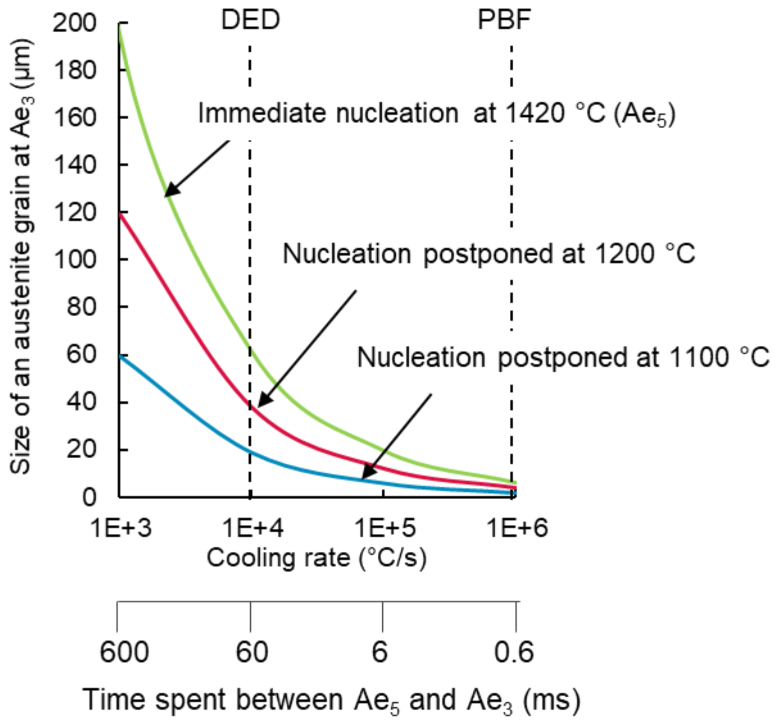

Figure 2: Size of an austenite grain when Ae_3 is reached, calculated with eq. (1) and eq. (3).

This model demonstrates the important effect of the cooling rate on the growth of an austenite grain: the faster the cooling rate, the less time the new austenite grain will have time to grow.

Two cooling rates representative of PBF-LB and DED-LB can be considered, according to the correlation set by Ma et al. [14], to illustrate the impact of the cooling rate on microstructures. In DED-LB ($v = 10^4$ °C/s), the size of an austenite grain can theoretically reach 61 µm. The time spent in the domains δ + γ and γ is therefore sufficient to allow the formation and growth of austenite grains, until the δ ferrite disappears completely.

In contrast, in PBF-LB ($v = 10^6$ °C/s) the time spent in the γ domain is 10 to 100 times shorter, leaving much less time for austenite grains to grow. With the cooling rate of 10^6 °C/s, an austenite grain only reaches a theoretical size of 6 µm if nucleation starts at Ae_5 and can go down to 1.9 µm if the nucleation stage is delayed to lower temperature. This demonstrates that a very high cooling rate can lower the formation of austenite and then martensite in Fe-9Cr-1Mo.

The austenite formation and growth stop when the Ae_3 temperature is reached. From this temperature, the untransformed δ ferrite becomes stable again up to room temperature. Any austenite grains that may have formed are transformed into martensite when the Ms temperature is reached (around 400 °C).

From the calculations made, an original CCT (Continuous Cooling Transformations) diagram starting from the δ phase is proposed (Figure 3).

For a fast PBF-LB cooling, austenite only has little time to form so the most of the δ ferrite is maintained up to room temperature. For a DED-LB cooling, or slower cooling, such as a conventional water quench, austenite replaces the δ ferrite and forms martensite at room temperature.

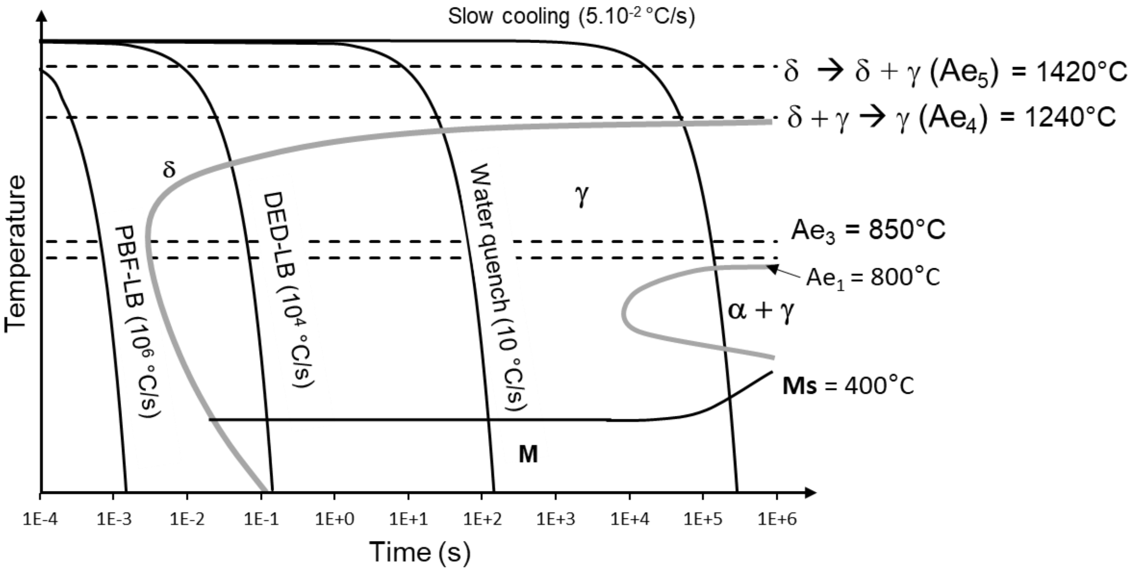

Figure 3: Schematic CCT diagram of the Fe-9Cr-1Mo to report phases transformations in rapid cooling from the δ phase.

Some phenomena are not considered in this model and may further reduce the size of the austenite grains previously calculated. For example, the initial formation of the austenite nucleus may be delayed (due to chemical heterogeneities for example): for nucleation at 1100 °C instead of 1420 °C, with a cooling rate of 10^6 °C/s, the size of the austenite grain when Ae_3 is reached is only 1.9 µm (blue curve Figure 2). The possibility of forming such a segregation during solidification will be discussed in the next section. This model also does not consider capillarity, or precipitates formation (like $M_{23}C_6$), which could further slow the growth of austenite.

4. DISCUSSION AND ANALYSIS OF EXPERIMENTAL OBSERVATIONS

4.1 Segregation effects during the solidification

In paragraph 3, it is assumed that all the liquid is transformed into delta ferrite with the same composition to simplify the explanation of the model. In practical cases, it is known that fast solidification implies segregation [22,23].

It is possible to consider the chemical segregation in the model, by using the phase diagram associated with the composition between and inside the solidification cell (it is the diagrams showed in Figure 5, with a correction considering the diffusion in solid delta phase as shown in Figure 6) instead of using the general Fe-9Cr-1Mo phase diagram (Figure 1).

The purpose of this paragraph is not to show the application of the model in this case, but to show that segregation phenomena only really has an impact in PBF and can only limit the formation of austenite.

The very fast cooling undergone in additive manufacturing leads to an out-of-equilibrium solidification of the liquid. Under these conditions, the diffusion of the metallic elements in the solid is not fast enough to guarantee chemical homogeneity. On the other hand, the solid/liquid interface velocity is not fast enough to deviate from the local thermodynamic equilibrium [24]. For most of the alloying elements used in steel, this implies that the solid formed at the end of solidification will be enriched compared to the solid formed at the beginning with partition coefficient k, defined as the ratio between the solid to the liquid composition, smaller than 1. The Gulliver-Scheil equations [25] can be used to account for this enrichment and to predict possible changes in the solidification sequence.

In the following, the solidification microstructure is assumed to be cellular rather than dendritic. The considered length scale for microsegregation is half the cellular spacing $\lambda/2$ (Figure 4(a)), it can be estimated using the geometrical model developed by Hunt [26], that has already been successfully applied to predict spacing in AM solidification microstructure [27]. Calculations lead to values of λ of 2 µm for DED-LB and 0.5 µm for PBF-LB. Experimentally, the measured solidification cell size is typically 1 to 5 µm in diameter, depending on the process and parameters used [14]. The small size of the solidification cells makes it difficult to experimentally observe compositional differences. The analysed surface in SEM-EDX is generally in the range of 0.1 pt/µm [28], which is too large to measure the chemical segregations induced by such solidification, STEM-EDX should be used for this purpose as done in [23] for example.

As assumed at the beginning of section 3, the Scheil equation predicts that all the solidification occurs in δ ferrite (Figure 4(b)), despite the compositional differences that can be observed in the solid between the beginning and the end of solidification (Figure 4(c)).

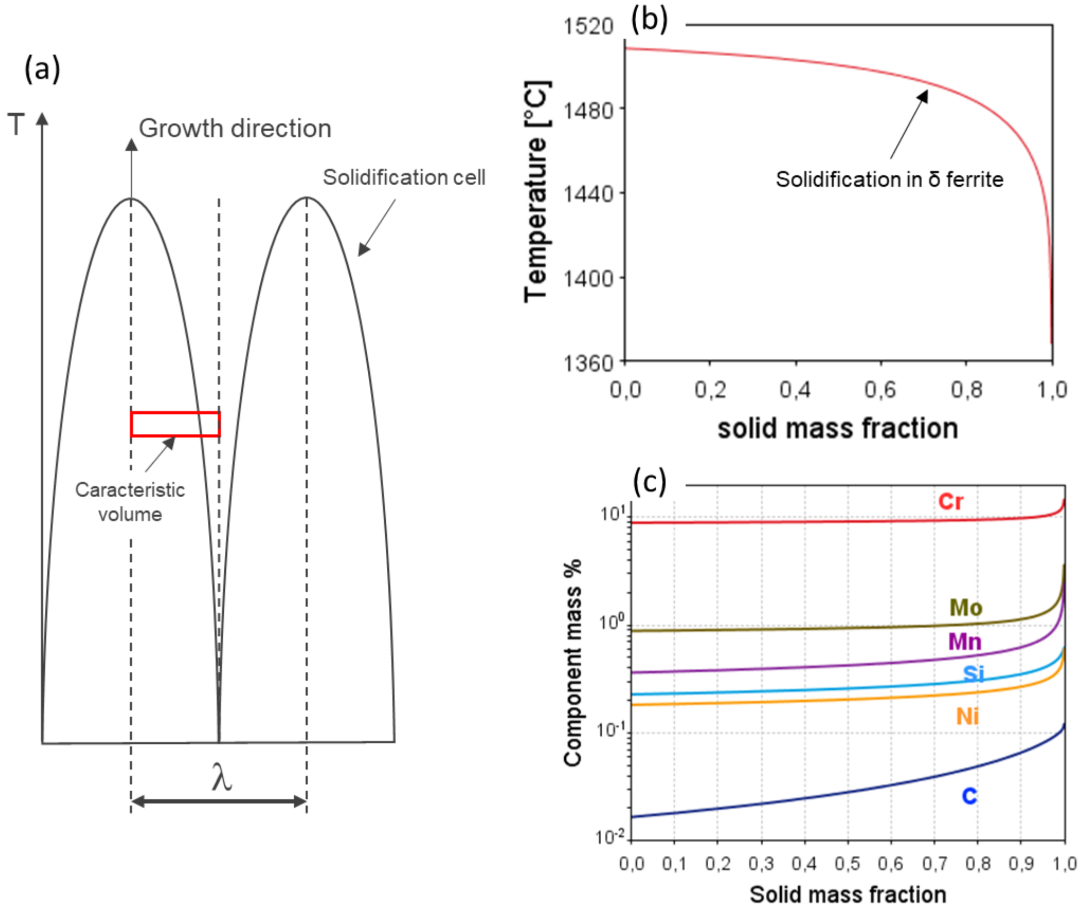

Figure 4: (a) Scheme of the solidifying cellular structure with the considered characteristic volume, (b) Solidification sequence in Fe-9Cr-1Mo steel, (c) solid chemical composition evolution during solidification. Computed with ThermoCalc (TCFE5 database) according to Gulliver-Scheil equations.

Such local differences in chemistry between the solid formed at the beginning and at the end of solidification (i.e. between the interior and the edge of the solidification cells) have already been observed in the literature, especially in 316L after PBF-LB [22,23] or DED-LB [29] and also in 300M low alloyed steel (40 NiSiCrMo 7) [30].

It would be possible to calculate the phase change temperatures during the cooling of each of the compositions of the solid formed during solidification. As the composition of the solid varies little, up to the last fractions of solid formed, we have chosen for simplicity, to represent only the two extreme compositions corresponding to the first and the last solid formed (Figure 5).

At the beginning of solidification, the composition of the solid is close to the nominal composition, the liquid solidifies into δ ferrite and can then be transformed into austenite at lower temperatures (Figure 5 (a)). At the end of solidification, the solid formed is enriched in alloying elements such as Cr, C, Mo and Mn (Figure 5 (b)). In this case, the liquid is still transformed into δ ferrite but these changes in chemical composition stabilize the ferrite and prevent the formation of austenite at lower temperatures (Figure 5 (b)). However, this more strongly ferrite-forming composition only affects a few percent of the solid formed at the end of solidification.

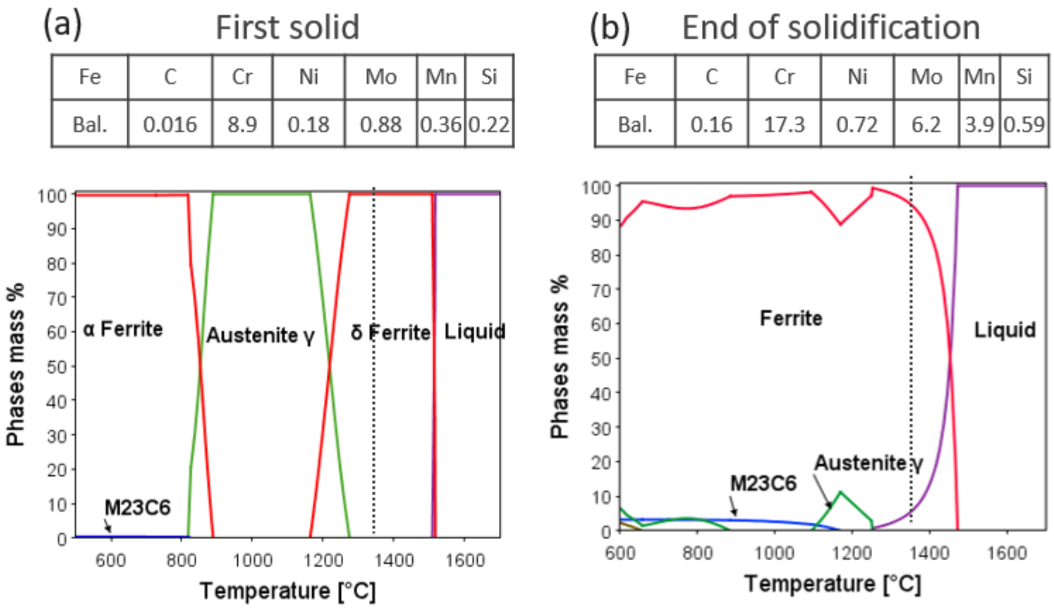
(a) First solid

Fe	C	Cr	Ni	Mo	Mn	Si
Bal.	0.016	8.9	0.18	0.88	0.36	0.22

(b) End of solidification

Fe	C	Cr	Ni	Mo	Mn	Si
Bal.	0.16	17.3	0.72	6.2	3.9	0.59

Figure 5: Compositions and equilibrium property diagrams of the solid composition at the beginning (a) and at the end (b) of solidification.

These theoretical equilibrium calculations show that it is possible to form austenite on cooling in the majority of the solidified material, the driving force to form austenite decreases while the solid is enriched with solute elements. However, since cooling in additive manufacturing is extremely rapid, it is necessary to consider the kinetic aspects of the δ→γ phase change to understand the ferritic/martensitic microstructures obtained in additive manufacturing, as it was proposed in the previous section.

Around 1360 °C, the δ phase solidification is complete and chemical segregations exist between the solid at the edge of the solidification cells, formed last, and the rest of the solid.

Between 1360 °C and 1250 °C, the δ ferrite is stable (Figure 5). It can be noticed that in this case Ae_5 is lowered with respect to the calculation performed without segregation in section 3, were Ae_5 = 1420 °C. In this temperature range, the segregations formed during solidification can be partially homogenized by diffusion. Using the well-known formula giving for a time interval dt and a temperature-dependent diffusion coefficient *D(T)*, the characteristic diffusion length *dL* of a chemical element, it is possible to evaluate the effectiveness of homogenization in this temperature range:

$$\boldsymbol{dL = \sqrt{D(T).dt}} \tag{4}$$

For a temperature increment *dT* and a given cooling speed *v*, the time spent at this temperature is expressed as:

$$\boldsymbol{dt = \frac{dT}{v}} \tag{5}$$

Combining (4) and (5), it is possible to compute for each temperature increment the diffusion length increment. Summing these increments allows to calculate the diffusion length in a temperature range for a given cooling rate:

$$\boldsymbol{L = \int dL = \int \left(D(T).\frac{dT}{v}\right)^{0.5}} \tag{6}$$

As carbon is an interstitial element, its diffusion is much faster than that of substitutional metallic elements such as chromium or molybdenum. Here, only diffusion of carbon and chromium are considered. Chromium is chosen to represent the diffusion of the substitutional elements because it is the element that is present in the largest quantity in Fe-9Cr-1Mo. Together with carbon, it is mainly responsible for the control of the ferrite ↔ austenite transformation in this alloy.

For carbon, with a cooling rate of 10^6 °C/s (PBF-LB), the characteristic diffusion length is greater than the size of the solidification cells ($L_{C,\ PBF\text{-}LB}$ = 5.7 µm compared with $\lambda_{PBF\text{-}LB}/2$ = 0.25 µm, and $L_{c,DED\text{-}LB}$ = 57 µm compared with $\lambda_{DED\text{-}LB}/2$ = 1 µm) (Figure 6 (a)). This shows that the diffusion of carbon in the δ domain is fast enough to ensure complete homogenization across the solidification cells, whether in DED-LB or PBF-LB.

For chromium, diffusion is slower. At a cooling rate of 10^6 °C/s (PBF-LB) the diffusion length is roughly the size of the solidification cells ($L_{Cr,\ PBF\text{-}LB}$ = 0.21 µm to be compared with $\lambda_{PBF\text{-}LB}/2$ = 0.25 µm), which means that Cr segregations probably still remain marked at the edge of the solidification cells when entering the austenitic domain. However, at a velocity of 10^4 °C/s (DED-LB), the characteristic diffusion length is larger than the size of the solidification cells ($L_{Cr,\ DED\text{-}LB}$ = 2.1 µm to be compared with $\lambda_{DED\text{-}LB}/2$ = 1 µm), which means that the Cr segregations between the cells are attenuated during this cooling phase.

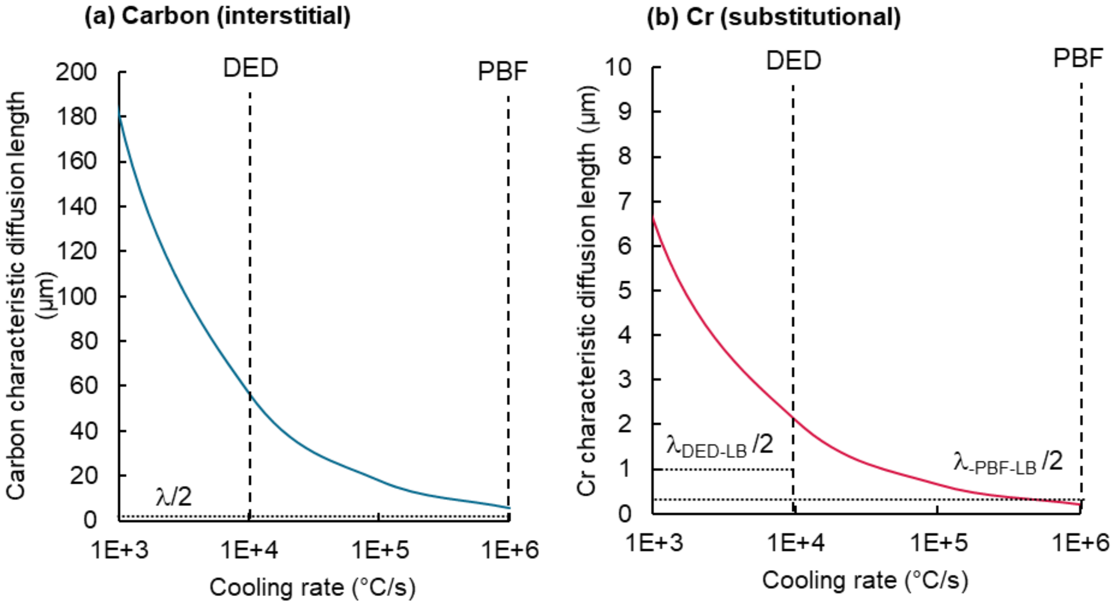

Figure 6: Characteristic diffusion length between 1360 °C and 1250 °C (δ phase) for (a) carbon and (b) chromium. Diffusion coefficients in δ phase are extracted from MOB2 ThermoCalc database.

At the end of solidification and cooling in the δ domain, most of the solid formed has a chemical composition that allows the formation of austenite. Only a few percent of the PBF-LB solid still has a ferrite-forming composition. It is usually admitted that the austenite nucleation is favored on defects, such as at the grain boundaries and intergranular solidification cells [31,32]. In the case of the PBF-LB Fe-9Cr-1Mo, the chemical composition at these places favors the stabilization of the ferrite because of the Cr enrichment. Austenite nucleation should be more difficult because of this enrichment in PBF-LB, this may result in a delay in austenite nucleation and therefore in retention of δ ferrite at room temperature.

4.2 Analysis of powder microstructures

Powder microstructure was analyzed on polished cross section by EBSD (Figure 7). It is interesting to note that the microstructure is changing with the powder size: small particles are ferritic (Figure 7(a)) and large particles are martensitic (Figure 7(c)). There is a critical size for which it is possible to observe ferritic-martensitic structures (Figure 7(b)).

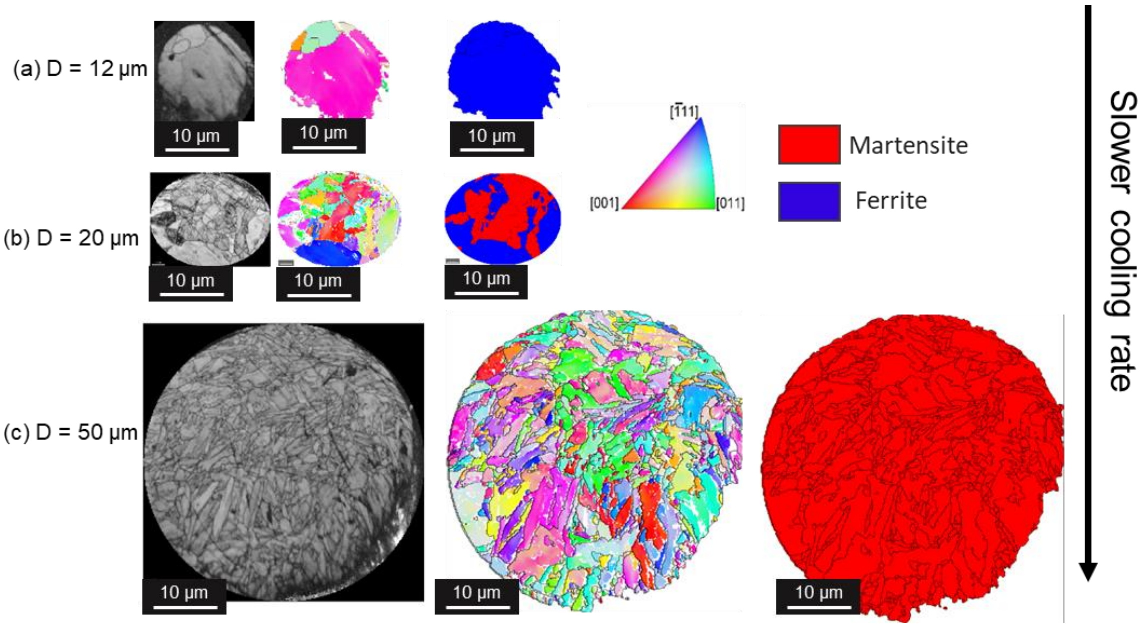

Figure 7: Different microstructures of the Fe-9Cr-1Mo powder (EBSD band contrast, IPF, and phase map): (a) a small ferritic particle, (b) a ferritic/martensitic particle and (c) a fully martensitic particle.

Such microstructure changes in steel powders are not particularly common in the literature. However, in 2002, Pryds and Pedersen [33] observed this phenomenon in a martensitic powder of X20 CrMoV 12-1 steel. To explain this result, the authors estimated the cooling rate of the powder particles as a function of their size. According to their calculations, a powder particle with a diameter around 10 µm is cooled at a speed of about 4.10^5 °C/s while a powder particle with a diameter around 50 µm is cooled at a speed of about 2.10^4 °C/s. This calculation shows that the size of the powder grain has a strong influence on the cooling rate.

Observations and these calculations agree with the model presented in section 3: in fast solidification conditions, the faster the Fe-9Cr-1Mo cools (i.e. the smaller the powder), the less martensite is formed. In their study, Pryds and Pedersen showed that austenite formed more easily in large diameter powders. This is because the higher number of grains and the slower cooling rate facilitate the germination of austenite in these powders. In small diameter powders, the lower grain count and faster cooling rate prevent austenite formation when cooling from liquid, which leads to a ferritic microstructure from the δ ferrite formed during solidification. This observation made in X20 CrMoV 12-1 steel can be extrapolated to the Fe-9Cr-1Mo steel studied here.

This demonstrates that for this chemical composition, the formation of the martensitic microstructure from the liquid phase is sensitive to the cooling rate between 10^4 °C/s and 10^5 °C/s.

However, it is important to keep in mind that powder particles are fully melted and mixed during the PBF-LB and DED-LB processes, meaning that their initial microstructure and eventual chemical segregations are erased during the building process.

4.3 Characterization of additive manufacturing microstructures

4.3.1 DED-LB

DED-LB microstructure at the top and in the middle of the wall was analysed by EBSD (Figure 8). These EBSD maps indicate that DED-LB samples are fully martensitic. This martensitic microstructure agrees with the model presented in section 3.

Prior austenite grains were determined using Kurdjumow-Sachs and Nishiyama-Wassermann relationships, with a method similar to the one used in ARPGE software [34]. This allows to plot prior austenite grains boundaries (in white on Figure 8 (c) and (f)), and to compute prior austenite grain size.

Analysis of the prior austenitic grains calculated by this method (in white Figure 8 (c) and (f)) shows that their size is higher at the top of the wall (average $D_{\gamma,}$ = 75 µm Figure 8 (c)) than at the bottom (average D_{γ} = 35 µm Figure 8 (f)). Since the real thermal cycle undergone by the material during the building is not precisely measured in this case, it is not possible to compare the grain sizes obtained here with the ones computed in section 3. Only the order of magnitude could be compared.

The increase in prior austenite grain size between the bottom and the top of the wall is explained by an increase of the temperature around the melt pool, as the height of the wall increases (cooling by conduction is reduced and the energy supplied by the laser accumulates) [12]. This increase in temperature is also accompanied by a reduction of the cooling rate. As the cooling rate decreases, the austenite nucleation is reduced. The temperature increase accelerates grain growth, leading to a higher austenite grain size at the top of the wall.

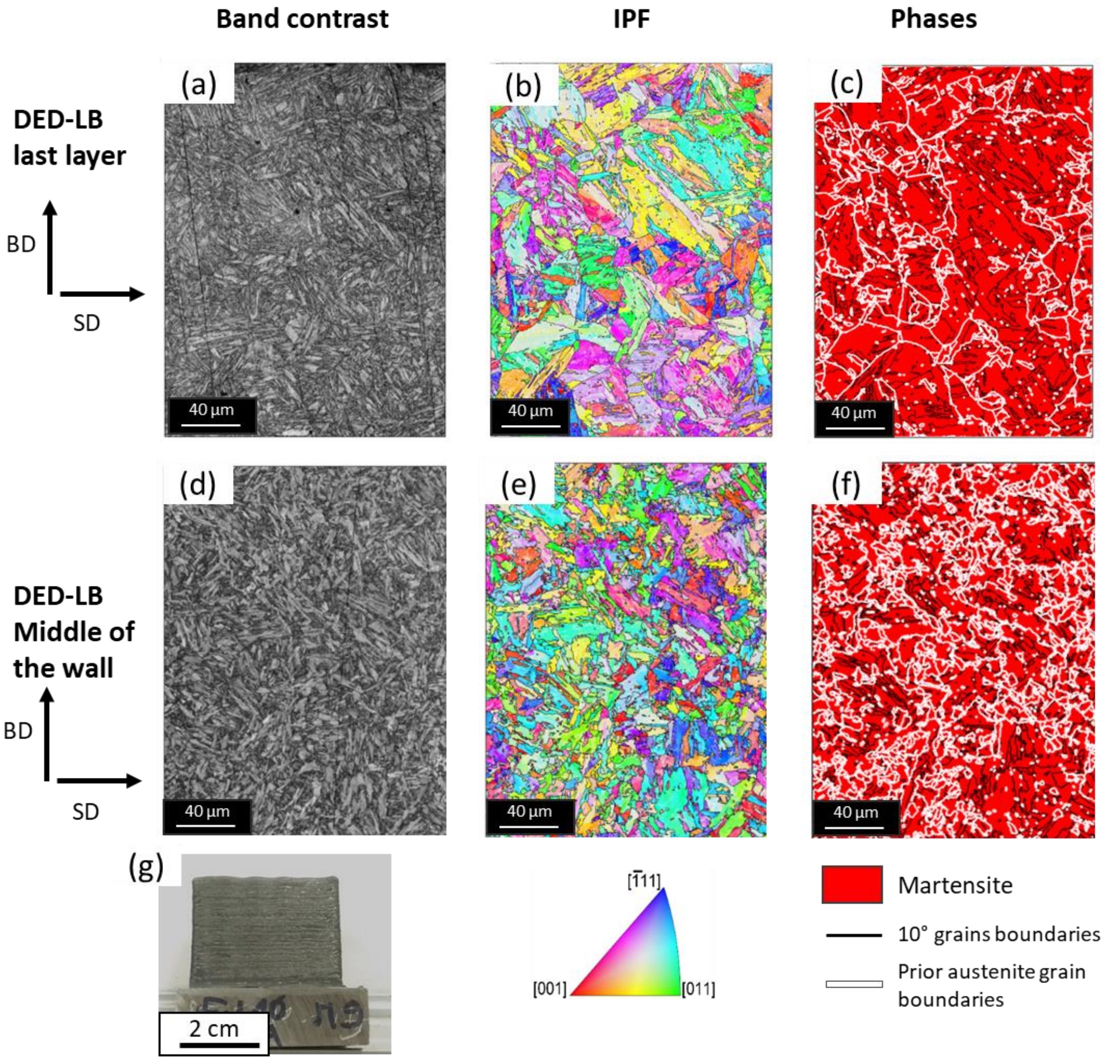

Figure 8: EBSD analysis of DED-LB sample, (a), (b) and (c) show the microstructure in the top layer, and (d) (e) and (f) show the microstructure in the middle of the wall. (g) is the DED-LB sample as built. Both are fully martensitic.

4.3.2 PBF-LB

In PBF-LB, the cooling rate during construction is higher than in DED-LB (approx. 10^6 °C/s in PBF-LB compared to 10^4 °C/s in DED-LB [14]). The increased cooling rate results in a more complex ferritic/martensitic microstructure (Figure 9(c)), which is unusual for bulk materials of equivalent composition.

In the middle of the wall, the ferrite forms coarse grains elongated in the building direction (BD), and characterized by a <001>//BD preferential orientation (red in Figure 9 (b)), which corresponds to the preferential solidification direction in cubic materials [35]. On this EBSD map, the size of the prior austenitic grains, determined in the same way as in Figure 8, is around 10 μm, which is much finer than in DED-LB.

The EBSD observation being a local observation, several large EBSD maps or optical micrograph are required to obtain a representative observation of the microstructure. Only the last layers are shown here in order to illustrate and validate the model presented.

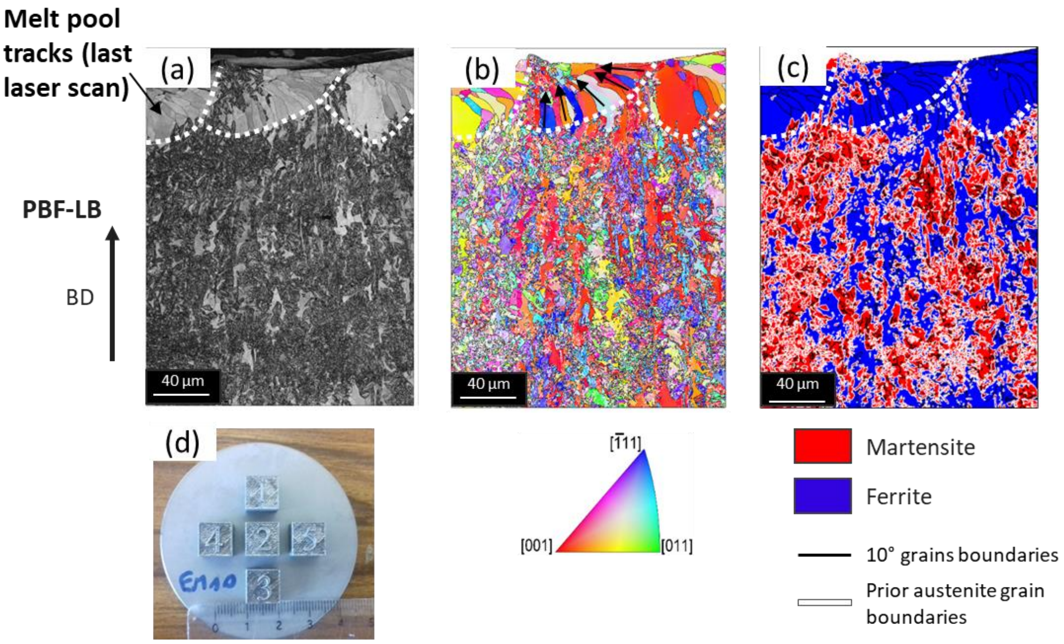

Figure 9: EBSD map of PBF-LB sample. The last melted layer is seen at the top of the map, melt pool tracks are visible on this last layer (dotted line). (a) Band contrast map, (b) IPF map projected along building direction (BD), arrows highlight the grain's direction change because of the thermal gradient and (c) phase map. (d) is a view of the as built samples.

Detailed analysis of the last layer shows a majority of ferritic grains (Figure 9 (c)). These ferritic grains are oriented in the direction of the thermal gradient of the last laser pass (arrows in Figure 9 (b)). A few martensite grains can be observed in this last layer, in the overlap zone between the melt pools (dotted lines in Figure 9). These observations show that martensite in PBF-LB materials is formed during the heating and subsequent cooling of the material induced by the construction of the next or adjacent layer. The ferrite comes directly from the solidification of the material. This observation is in good agreement with the model presented in section 3, which predicts the microstructure to be almost fully ferritic.

At the end of the first cooling cycle, the construction of the next layer causes a new heating/cooling cycle of the material and a repetition of all or part of the transformations seen previously. The areas close to the laser (above the blue line in Figure 10) will be melted and form the δ phase on cooling. The areas further away remain in the solid state (between the blue and red lines in Figure 10), and spend more time in the austenitic range (heating + cooling): they are partially austenitized and may form martensite on cooling. Below the red line in Figure 10, the time spent in the austenitic domain during the cycle is no longer sufficient to form austenite, and the δ ferrite does not transform.

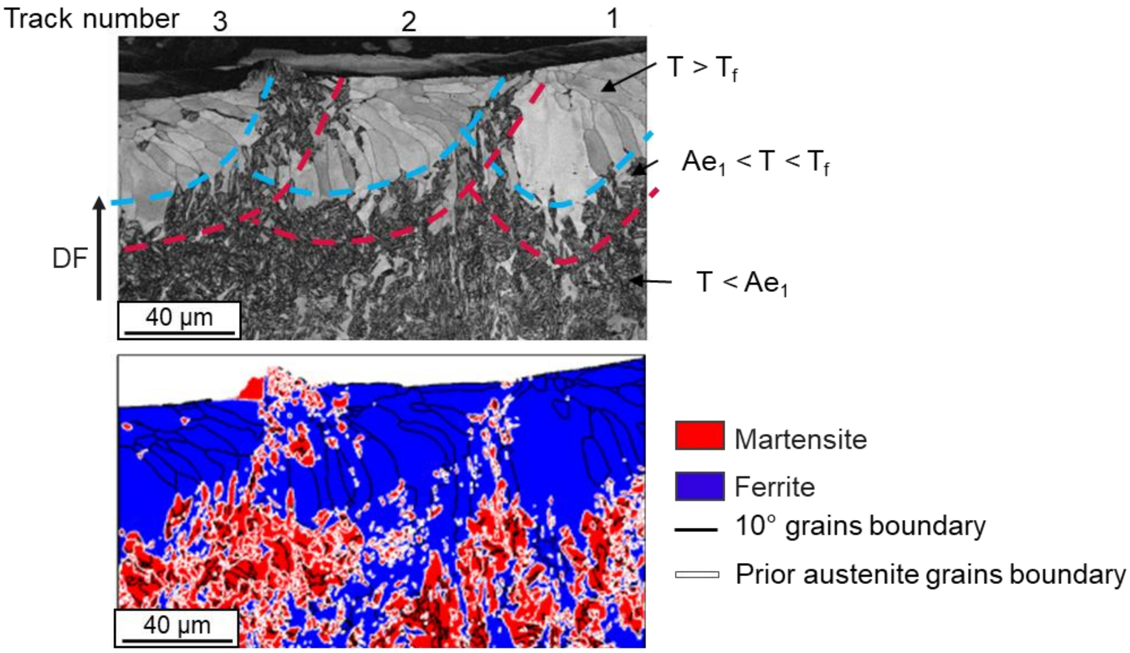

Figure 10: Scheme of liquid to δ, δ to γ, and γ to α transformation isotherms to explain the formation of martensite between the melts pool and below the last melt track.

In the proposed scenario, the martensite observed in the rest of the PBF-LB sample is formed during the successive anneals caused by the construction of the upper layers. During these anneals, the time spent in the austenitic domain can be twice as long due to heating and cooling of the material, and the chemical segregation of the solidification is less marked, making nucleation easier. It is not showed in this paper but it is possible to use the formulas presented previously to predict the size of a nucleus formed during the second, third etc. thermal cycle, the only difference is that the time considered in the γ domain is different (longer at the second thermal cycle). If the time spent in the gamma domain is twice longer, the grain size will be $\sqrt{2}$ larger. This leads to the formation of large amounts of austenite and then martensite in the sample bulk.

4.4 Other examples from literature

With the cooling rate, the chemical composition also has a strong effect on as built microstructures. The chemical composition controls both the solidification sequence and the size of the austenitic domain, and thus the time spent in the austenitic domain during cooling.

In this way, Vuunam et al. [8] showed that with constant manufacturing parameters, it is possible to increase the proportion of δ ferrite in 17-4PH (precipitation hardened martensitic steel) by increasing the initial Cr_{eq} / Ni_{eq} ratio in powder. These authors obtained a material with 90 % of ferrite for a Cr_{eq}/Ni_{eq} ratio of 2.81, which is smaller to that of the Fe-9Cr-1Mo used here (Cr_{eq}/Ni_{eq} = 3.0). In their experiment, the surface energy used for building is likely to be smaller (around 5 J/mm² versus 10 J/mm² here), which leads to a cooling rate that can be two to three times higher in their process, and therefore to a microstructure containing much more ferrite. In their experiment, the time spent in the austenitic domain is so small that even the reheating induced by the building of the next layers is not sufficient to allow the formation of austenite. By reducing the Cr_{eq}/Ni_{eq} ratio, they succeeded to widen the austenitic domain and produce almost fully martensitic samples with the same building parameters.

In the same way, with a more ferrite-forming composition, the δ ferrite is maintained more easily. For example, Gao et al. [32] obtained high fractions of δ ferrite in a Fe-9Cr-1W (around 30 %), for much lower cooling rates (10^2 °C/s) because their alloy contains half as much carbon as the one used here.

A slight variation in chemical composition can also alter the rapid solidification sequence and allow the appearance of austenite at the end of solidification, which then facilitates the disappearance of the ferrite δ. This is the case for example for the Fe-9Cr-1W of Sam et al. [36].

5. CONCLUSIONS

A scenario is proposed to explain differences observed in literature for the microstructure of martensitic steels after additive manufacturing. It is based on the calculation of the growth kinetics of austenite grains formed during cooling, as a function of the cooling rate. It explains why under certain conditions, martensite or ferrite is observed in the final microstructures. This model was successfully applied to the specific composition of a Fe-9Cr-1Mo steel, used in this work as an example. This approach could be used for other compositions of martensitic steels. Each step of the cooling process must be carefully checked, as the solidification path and the different equilibrium temperatures are very sensitive to the composition of the material.

This scenario shows that austenite nuclei may have more difficulty to form with PBF-LB due to the chemical segregation between the solidification cells. Then, the austenite grains do not have the time to grow. In contrast, in DED-LB, the time spent into the austenitic domain is longer, allowing austenite to grow and replace the δ ferrite formed at solidification.

It should be noted that these calculations show that the appearance of δ ferrite in PBF-LB for martensitic steels is very sensitive to the cooling rate, but also to the chemical composition. Indeed, the chemical composition controls both the solidification sequence and the size of the austenitic domain, and therefore the time spent in the austenitic domain during cooling.

This study highlights the important effect of the rapid solidification and cooling rate experienced in additive manufacturing on martensitic steels microstructures. Finally, one other conclusion is that the time spent between Ae_5 and Ae_1, controls the final microstructure. This time can be tuned either by controlling the size of the domain, by changing the composition, or the cooling rate, with the building parameters.

This understanding is one more step toward the control of microstructure and properties of additively manufactured martensitic steels, by a wise choice of the process and its parameters in phase with the alloy chemical composition. Finally, this approach can also be applied to alloys, other than martensitic steels, with several high temperature phase changes.

6. ACKNOWLEDGEMENTS

Authors would like to thank Patrice Peyre and Thierry Malot (PIMM Laboratory, Arts et Métiers ParisTech) for their expertise and their help in the production of the DED-LB samples used for this study, Fernando Lomello (CEA-Saclay) for his help in the production of the PBF-LB samples and Elodie Rouesne (CEA-Saclay) for her help in EBSD acquisition and analysis.

7. BIBLIOGRAPHY

[1] C. Pandey, A. Giri, M.M. Mahapatra, Effect of normalizing temperature on microstructural stability and mechanical properties of creep strength enhanced ferritic P91 steel, Mater. Sci. Eng. A. 657 (2016) 173–184. https://doi.org/10.1016/j.msea.2016.01.066.

[2] V. Shankar, M. Valsan, K.B.S. Rao, R. Kannan, S.L. Mannan, S.D. Pathak, Low cycle fatigue behavior and microstructural evolution of modified 9Cr-1Mo ferritic steel, Mater. Sci. Eng. A. 437 (2006) 413–422. https://doi.org/10.1016/j.msea.2006.07.146.

[3] S.J. Zinkle, G.S. Was, Materials challenges in nuclear energy, Acta Mater. 61 (2013) 735–758. https://doi.org/https://doi.org/10.1016/j.actamat.2012.11.004.

[4] C. Cabet, F. Dalle, E. Gaganidze, J. Henry, H. Tanigawa, Ferritic-martensitic steels for fission and fusion applications, J. Nucl. Mater. 523 (2019) 510–537. https://doi.org/10.1016/j.jnucmat.2019.05.058.

[5] D. Herzog, V. Seyda, E. Wycisk, C. Emmelmann, Additive manufacturing of metals, Acta Mater. 117 (2016) 371–392. https://doi.org/10.1016/j.actamat.2016.07.019.

[6] Y. Sun, R.J. Hebert, M. Aindow, Effect of laser scan length on the microstructure of additively manufactured 17-4PH stainless steel thin-walled parts, Addit. Manuf. 35 (2020) 101302. https://doi.org/10.1016/j.addma.2020.101302.

[7] A.A. Adeyemi, E. Akinlabi, R.M. Mahamood, K.O. Sanusi, S. Pityana, M. Tlotleng, Influence of laser power on microstructure of laser metal deposited 17-4 ph stainless steel, IOP Conf. Ser. Mater. Sci. Eng. 225 (2017) 012028. https://doi.org/10.1088/1757-899X/225/1/012028.

[8] S. Vunnam, A. Saboo, C. Sudbrack, T.L. Starr, Effect of powder chemical composition on the as-built microstructure of 17-4 PH stainless steel processed by selective laser melting, Addit. Manuf. 30 (2019) 100876. https://doi.org/10.1016/J.ADDMA.2019.100876.

[9] C.Y. Liu, J.D. Tong, M.G. Jiang, Z.W. Chen, G. Xu, H.B. Liao, P. Wang, X.Y. Wang, M. Xu, C.S. Lao, Effect of scanning strategy on microstructure and mechanical properties of selective laser melted reduced activation ferritic/martensitic steel, Mater. Sci. Eng. A. 766 (2019) 138364. https://doi.org/10.1016/j.msea.2019.138364.

[10] M.G. Jiang, Z.W. Chen, J.D. Tong, C.Y. Liu, G. Xu, H.B. Liao, P. Wang, X.Y. Wang, M. Xu, C.S. Lao, Strong and ductile reduced activation ferritic/martensitic steel additively manufactured by selective laser melting, Mater. Res. Lett. 7 (2019) 426–432. https://doi.org/10.1080/21663831.2019.1631224.

[11] W. Zhong, N. Sridharan, D. Isheim, K.G. Field, Y. Yang, K. Terrani, L. Tan, Microstructures and mechanical properties of a modified 9Cr ferritic-martensitic steel in the as-built condition after additive manufacturing, J. Nucl. Mater. (2020) 152742. https://doi.org/10.1016/j.jnucmat.2020.152742.

[12] Z. Xia, J. Xu, J. Shi, T. Shi, C. Sun, D. Qiu, Microstructure evolution and mechanical properties of reduced activation steel manufactured through laser directed energy deposition, Addit. Manuf. 33 (2020) 101114. https://doi.org/10.1016/j.addma.2020.101114.

[13] M. Alnajjar, F. Christien, K. Wolski, C. Bosch, Evidence of austenite by-passing in a stainless steel obtained from laser melting additive manufacturing, Addit. Manuf. 25 (2019) 187–195. https://doi.org/10.1016/j.addma.2018.11.004.

[14] M. Ma, Z. Wang, X. Zeng, A comparison on metallurgical behaviors of 316L stainless steel by selective laser melting and laser cladding deposition, Mater. Sci. Eng. A. 685 (2017) 265–273. https://doi.org/10.1016/j.msea.2016.12.112.

[15] M.M. Nowell, S.I. Wright, J.O. Carpenter, Differentiating ferrite and martensite in steel microstructures using electron backscatter diffraction, Mater. Sci. Technol. Conf. Exhib. 2009, MS T’09. 2 (2009) 933–943.

[16] L. Mujica, S. Weber, H. Pinto, C. Thomy, F. Vollertsen, Microstructure and mechanical properties of laser-welded joints of TWIP and TRIP steels, Mater. Sci. Eng. A. 527 (2010)

2071–2078. https://doi.org/10.1016/j.msea.2009.11.050.

[17] A.W. Wilson, G. Spanos, Application of orientation imaging microscopy to study phase transformations in steels, Mater. Charact. 46 (2001) 407–418. https://doi.org/10.1016/S1044-5803(01)00140-1.

[18] C.L. Leone, H.W. Kerr, The Ferrite to Austenite Transformation in Stainless Steels, Weld. Res. 61 (1982) 13s-22s.

[19] S. Kobayashi, K. Sawada, T. Hara, H. Kushima, K. Kimura, The formation and dissolution of residual δ ferrite in ASME Grade 91 steel plates, Mater. Sci. Eng. A. 592 (2014) 241–248. https://doi.org/10.1016/j.msea.2013.10.058.

[20] H. Hemmer, Grong, A process model for the heat-affected zone microstructure evolution in duplex stainless steel weldments: Part I. The model, Metall. Mater. Trans. A Phys. Metall. Mater. Sci. 30 (1999) 2915–2929. https://doi.org/10.1007/s11661-999-0129-2.

[21] S. Hertzman, P.J. Ferreira, B. Brolund, An experimental and theoretical study of heat-affected zone austenite reformation in three duplex stainless steels, Metall. Mater. Trans. A Phys. Metall. Mater. Sci. 28 (1997) 277–285. https://doi.org/10.1007/s11661-997-0130-6.

[22] L. Liu, Q. Ding, Y. Zhong, J. Zou, J. Wu, Y.L. Chiu, J. Li, Z. Zhang, Q. Yu, Z. Shen, Dislocation network in additive manufactured steel breaks strength-ductility trade-off, Mater. Today. 21 (2017) 354–361. https://doi.org/10.1016/j.mattod.2017.11.004.

[23] M. Godec, S. Zaefferer, B. Podgornik, M. Šinko, E. Tchernychova, Quantitative multiscale correlative microstructure analysis of additive manufacturing of stainless steel 316L processed by selective laser melting, Mater. Charact. 160 (2020) 110074. https://doi.org/10.1016/j.matchar.2019.110074.

[24] M.J. Aziz, T. Kaplan, Continuous growth model for interface motion during alloy solidification, Acta Metall. 36 (1988) 2335–2347. https://doi.org/https://doi.org/10.1016/0001-6160(88)90333-1.

[25] E. Scheil, Bemerkungen zur schichtkristallbildung, Zeitschrift Für Met. 34 (1942) 70–72.

[26] J.D. Hunt, Cellular and primary dendrite spacings, in: Proc. Int. Conf. Solidif., London Metals Society, Sheffield, England, 1979: pp. 3–9.

[27] Y. Li, A. Olmedilla, M. Založnik, J. Zollinger, L. Dembinski, A. Mathieu, Solidification microstructure during selective laser melting of Ni based superalloy: Experiment and mesoscopic modelling, in: IOP Conf. Ser. Mater. Sci. Eng., IOP Publishing, 2019: p. 012004. https://doi.org/10.1088/1757-899X/529/1/012004.

[28] M. Moncel, Méthodes physiques d ' analyse en métallurgie, Tech. l'ingénieur. Matériaux (1991). http://cat.inist.fr/?aModele=afficheN&cpsidt=16443348.

[29] M. Ziętala, T. Durejko, M. Polański, I. Kunce, T. Płociński, W. Zieliński, M. Łazińska, W. Stępniowski, T. Czujko, K.J. Kurzydłowski, Z. Bojar, The microstructure, mechanical properties and corrosion resistance of 316 L stainless steel fabricated using laser engineered net shaping, Mater. Sci. Eng. A. 677 (2016) 1–10. https://doi.org/10.1016/j.msea.2016.09.028.

[30] F. Liu, X. Lin, J. Shi, Y. Zhang, P. Bian, X. Li, Y. Hu, Effect of microstructure on the Charpy impact properties of directed energy deposition 300M steel, Addit. Manuf. 29 (2019) 100795. https://doi.org/10.1016/J.ADDMA.2019.100795.

[31] R.-I. Hsieh, H.-Y. Liou, Y.-T. Pan, Effects of Cooling Time and Alloying Elements on the Microstructure of the Gleeble-Simulated Heat-Affected Zone of 22% Cr Duplex Stainless Steels, ASM International, 2001.

[32] Q. Gao, Y. Liu, X. Di, Z. Dong, Z. Yan, The isochronal δ → γ transformation of high Cr ferritic heat-resistant steel during cooling, J. Mater. Sci. 46 (2011) 6910–6915. https://doi.org/10.1007/s10853-011-5656-8.

[33] N.H. Pryds, A.S. Pedersen, Rapid solidification of martensitic stainless steel atomized droplets, Metall. Mater. Trans. A Phys. Metall. Mater. Sci. 33 (2002) 3755–3761. https://doi.org/10.1007/s11661-002-0248-5.

[34] C. Cayron, ARPGE: A computer program to automatically reconstruct the parent grains from electron backscatter diffraction data, J. Appl. Crystallogr. 40 (2007) 1183–1188.

https://doi.org/10.1107/S0021889807048777.

[35] T. Niendorf, S. Leuders, A. Riemer, H.A. Richard, T. Tröster, D. Schwarze, Highly Anisotropic Steel Processed by Selective Laser Melting, Metall. Mater. Trans. B. 44B (2013) 794–796. https://doi.org/10.1007/s11663-013-9875-z.

[36] S. Sam, C.R. Das, V. Ramasubbu, S.K. Albert, A.K. Bhaduri, T. Jayakumar, E. Rajendra Kumar, Delta ferrite in the weld metal of reduced activation ferritic martensitic steel, J. Nucl. Mater. 455 (2014) 343–348. https://doi.org/10.1016/j.jnucmat.2014.07.008.